Ultrastrong Coupling by Assembling Plasmonic Metal Oxide Nanocrystals in Open Cavities

Woo Je Chang[1], Benjamin J. Roman[1], Tanay Paul[1], Zarko Sakotic[2], Priyansh Vora[1], Kihoon Kim[1], Daniel Wasserman[2*], Thomas M. Truskett[1,3*], Delia J. Milliron[1,4*]

[1]McKetta Department of Chemical Engineering, University of Texas at Austin, Austin, Texas 78712, United States.

[2]Chandra Family Department of Electrical and Computer Engineering, University of Texas at Austin, Austin, Texas 78758, United States.

[3]Department of Physics, University of Texas at Austin, Austin, Texas 78712, United States.

[4]Department of Chemistry, University of Texas at Austin, Austin, Texas 78712, United States.

*Corresponding authors. Emails: `dw@utexas.edu` (D.W.), `truskett@che.utexas.edu` (T.M.T.), `milliron@che.utexas.edu` (D.J.M.)

Plasmon polaritons created by coupling optical cavity modes with plasmonic resonances offer widely tunable frequencies and strong light-matter interaction. While metallic nanocrystals (NCs) are compelling building blocks, existing approaches for their photonic integration are not scalable, limiting systematic study and potential applications. Here, we assemble colloidal tin-doped indium oxide NCs in a straightforward Salisbury screen configuration to realize an 'open' cavity structure, where the infrared resonance frequencies of the NC assembly and the photonic mode are independently controlled and strongly coupled. By modeling each NC layer as an effective medium, we designed cavities with plasmon-polariton spectra tuned to target frequencies, for example approximating the two atmospheric transparency windows. NCs with varying ligands and doping concentrations can be stacked in the assemblies to customize the spectral lineshape and control the spatial distribution of the electric near-field within

the assembly. We anticipate applications in chemosensing and photonic technologies.

Teaser

Strong coupling between colloidal nanocrystals and simple photonic cavities tunes the infrared resonance and electric field distribution.

Introduction

Through their designed resonances, photonic structures enable selective concentration of incident light within a confined modal volume, which can greatly enhance light's interaction with cavity-embedded materials through strong electric field coupling (*1*). This strong coupling leads to hybridization and the formation of new quantum states that are part light and part matter, known as polaritons. For sufficiently strong coupling and coherent energy exchange, these distinct polariton states are separated by a frequency difference known as a Rabi splitting. Creating polaritons provides access to resonant frequencies and effective transition dipole strengths beyond the intrinsic properties of the polarizable material (*2*), thereby offering opportunities for optoelectronic (*3*) and sensing applications (*4*).

Among optical excitations, plasmon resonance, driven by the oscillation of free charge carriers, is a prime candidate for forming polaritons owing to a large dipole strength, which favors strong coupling with photonic modes (*5–7*). For example, in metallic antenna arrays made by electron beam lithography, the localized surface plasmon resonance (LSPR) modes of the antennae are tuned by adjusting their dimensions to suitable frequencies for coupling to photonic resonators (*8–11*). The Fabry–Pérot (F-P) cavity is a prototypical photonic structure that enables independent control of plasmon and photonic mode resonances when integrated with these patterned metallic arrays (*8, 9*). Two closely spaced metal mirrors establish the resonant modes and confine the electric field, which can efficiently couple to LSPR modes of embedded nanorods. This coupling can lead to significant frequency splitting between two polariton modes, reaching the ultrastrong coupling regime, *i.e.* coupling strength (half of the Rabi splitting) exceeding 10% of the unperturbed resonant frequency. Under ultrastrong coupling conditions, exotic quantum behaviors emerge, such as imprinting the excited-state character of the photon onto the polariton's ground state or the materialization of

2

virtual states, enabling non-linear optical processes (*12*). This ultrastrong coupling regime has garnered interest for photoelectrochemistry (*13, 14*), photovoltaics (*15*), non-linear optics (*16, 17*), and modifying rates of chemical reactions (*18*). However, electron beam-patterned plasmonic metal structures require a laborious fabrication process, limiting systematic study and making scaled up production infeasible. Additionally, while three-dimensional integration can offer more degrees of freedom for optical design and enhancing the coupling strength, electron beam patterning is generally limited to two-dimensional fabricated structures.

Substituting electron-beam patterned plasmonic structures with assemblies of colloidal plasmonic nanocrystals (NCs) brings new design flexibility in the height dimension and may enable scalable fabrication of cavity-coupled plasmon-polaritonic architectures (*19–21*). In previous examples, the thickness of a NC assembly was itself used to form the optical path of a F-P cavity; refractive index contrast induces boundary reflections to establish optical modes, which can be enhanced by evaporating a metal cladding layer (*22*). In dense assemblies of NCs, coupling among their LSPR modes produces strong collective plasmon resonance (CPR) with a giant dipolar transition strength that makes them even more suitable than well-spaced antennae for coupling with cavity modes and realizing giant Rabi splitting (*20*). Beyond the fundamental interest in Rabi splitting, the CPR in compact NC assemblies also gives rise to strong electric field confinement within the NC gaps, creating hot spots for interactions with other optical components (*21, 23*). For instance, introducing molecules into the gaps between NCs leads to coupling between plasmon polaritons and molecular vibrations, resulting in significant surface-enhanced infrared (IR) absorption of molecular vibrations that boosts their extinction intensity for more sensitive chemodetection (*21, 23, 24*).

Yet, using metallic NCs as plasmonic building blocks for polariton formation poses challenges in tuning the resonance frequency, which is inextricably determined by the size and shape of the NCs (*25, 26*), thus constraining the material design parameters. In addition, when the photonic cavity is defined by the thickness of the NC assembly, the cavity mode tuning becomes discrete with the optical path length adjustable only in units of the NC size or spacing. Furthermore, the thickness can usually be precisely controlled only over local, micron scales, making it challenging to fabricate structures with a uniform optical response over larger areas. These limitations motivate a new approach in which the NCs and cavity are independently designed and fabricated, and the resonant frequencies of the plasmonic and photonic modes can be precisely varied to fully develop

3

the tunability of the spectral lineshapes of the plasmon-polaritons and to achieve uniform optical response over practical, large areas.

Here, we develop photonic structures that couple optical modes of open cavities with the CPR of assembled plasmonic metal oxide NCs. Doped metal oxides NCs, particularly tin-doped indium oxide (ITO) NCs, are solution processible for easy, scalable integration and their LSPR is synthetically tunable across the IR frequency range by adjusting the tin (Sn) doping concentration (*27*). In densely packed assemblies, ITO NCs exhibit defect-tolerant CPR properties and can function as metasurfaces, for example tuning the frequency and bandwidth of their epsilon-near-zero permittivity response (*28–30*). By integrating these ITO NC metasurfaces atop a dielectric spacer and metal back reflector, we recently showed that the CPR-photonic coupling concentrates the electric field within the NC monolayer, enabling perfect absorption at tunable IR wavelengths depending on NC size and doping concentration (*31*). Now, we build on this strategy by stacking the assemblies into the third dimension, achieving ultrastrong coupling with control of the spectral response and the spatial distribution of the near-field hot spots within the NC assemblies. Extensive tunability of optical properties is made possible by our convergent fabrication strategy, which combines independent fabrication and co-design of optimized plasmonic and photonic modes.

Results

Cavity-Coupled NC Assemblies

To explore the properties of cavity-coupled NC assemblies, ITO NCs are synthesized using a slow-injection method (*32*) where the dopant precursor composition (*i.e.*, Sn to In ratio) and injection volume control the NC LSPR frequency and size, respectively (Figure S1 and Table S1). By drop-casting a colloidal NC solution onto an antisolvent subphase (acetonitrile), ITO NCs are assembled into a compact, uniform NC monolayer, either retaining the native oleate ligands or replacing them with another ligand of choice dissolved in the subphase (*31, 33–35*). Following assembly at the liquid-air interface, the NC monolayer is transferred to the prepared substrate by draining the subphase. This streamlined synthesis-to-assembly process can be repeated multiple times (*36*) with either the same or different types of ITO NCs and ligand molecules, allowing control over the
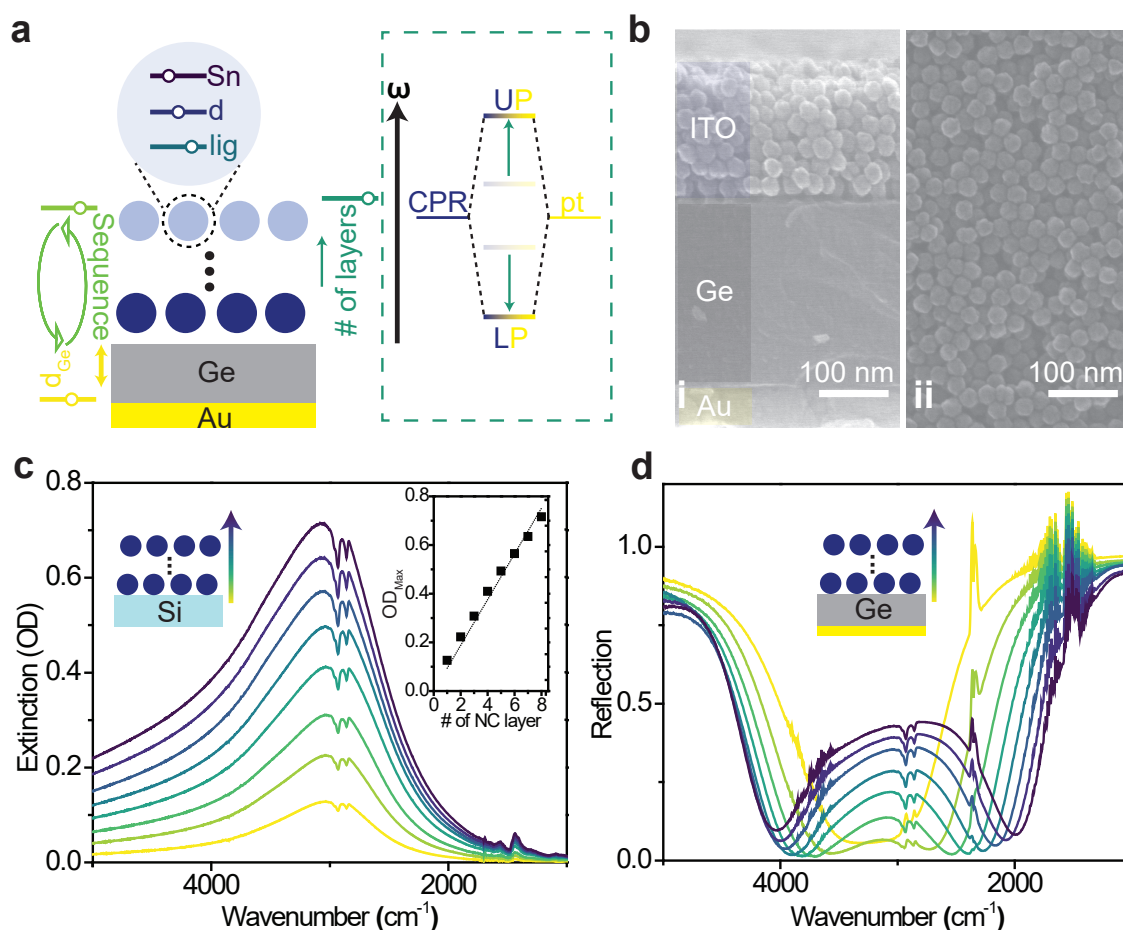
4

Figure 1: **Design of tunable cavity-coupled NC assemblies.** (a) Schematic of experimental tuning knobs including synthetically controlled parameters of the NC composition, the thickness of the Ge spacer, the NC assembly thickness, and the stacking sequence. The properties of the upper and lower polariton (UP and LP) modes resulting from coupling between the collective plasmon resonance (CPR) and photonic modes (pt) are adjusted based on these variables. (b) Scanning electron microscope (SEM) images of eight layers of 25 nm ITO NCs on a 215 nm Ge spacer layer and 100 nm Au layer. (i) Cross-sectional and (ii) top-down images. (c) Extinction spectra of 25 nm, 2.7% Sn ITO NCs as a function of the number of NC layers on an IR-transparent silicon wafer. Spectra for one to eight NC layers are shown. The inset shows the approximately linear dependence of the peak intensity of the extinction spectrum on the number of NC layers. (d) Reflection spectra of the stacks of the same ITO NCs in a Salisbury screen configuration, composed of 160 nm Ge and 100 nm Au.

5

number and sequence of NC layers and their surface functionality. In our current study, the substrate consists of an IR-transparent dielectric spacer layer (Ge) and metallic (Au) backing, known as the Salisbury screen configuration. The thickness of the germanium spacer (d_{Ge}) tunes the resonant frequency of the photonic mode, providing significant flexibility to couple to the CPR of the ITO NC assemblies (Figure 1a).

To demonstrate this concept, we iteratively prepared monolayers and stacked eight layers of 25 nm ITO NCs with a 2.7% Sn doping concentration onto a gold-germanium substrate (Figure 1b). These NCs are capped with oleate (OA) surface ligands, which adds about 3 nm to their effective diameter in building up the assembly's thickness (*37*) . Although the top-down scanning electron microscope (SEM) image of the NC assembly appears disordered, cross-sectional SEM images reveal eight NC layers on the Ge spacer layer. The thickness of the NC assembly is on average 213 (± 8) nm, which is closer to a simple linear scaling of the NC size (224 nm), than to the thinner assembly expected for perfect, close-packed three-dimensional ordering (183 nm). By varying the number of NC monolayers deposited on an IR-transparent substrate (double-side polished silicon), we observed an approximately linear increase in extinction peak intensity (Figure 1c, inset), with the peak frequency around 3000 cm^{-1} independent of the number of layers (Figure S2).

When we varied the number of NC layers in the Salisbury screen configuration, which consists of a germanium spacer layer (160 nm) and a thick gold backing (100 nm), much more pronounced changes appeared in the reflection spectra (Figure 1d). A NC monolayer exhibited a broad dip around 3000 cm^{-1}, indicating perfect absorption due to a resonantly coupled response of the NC CPR and the photonic cavity mode (*31*). For a bilayer of NCs, the single reflectance dip begins to split in two, and this splitting progressively increases with the number of NC layers. The increase in peak splitting with the addition of more of the polarizable medium (plasmonic NCs) indicates strong coupling between the photonic structure and the CPR of the NC layer (*38–40*). Therefore, we interpret these reflection dips as the upper polariton (UP) and lower polariton (LP), with the coupling between the photonic mode and CPR becoming more pronounced as additional NC layers are added to the Salisbury screen configuration, inducing a larger Rabi splitting between the UP and LP.

The development of well-defined polariton modes occured despite the structural disorder of the NC assemblies apparent in the SEM images, which we sought to understand by conducting optical
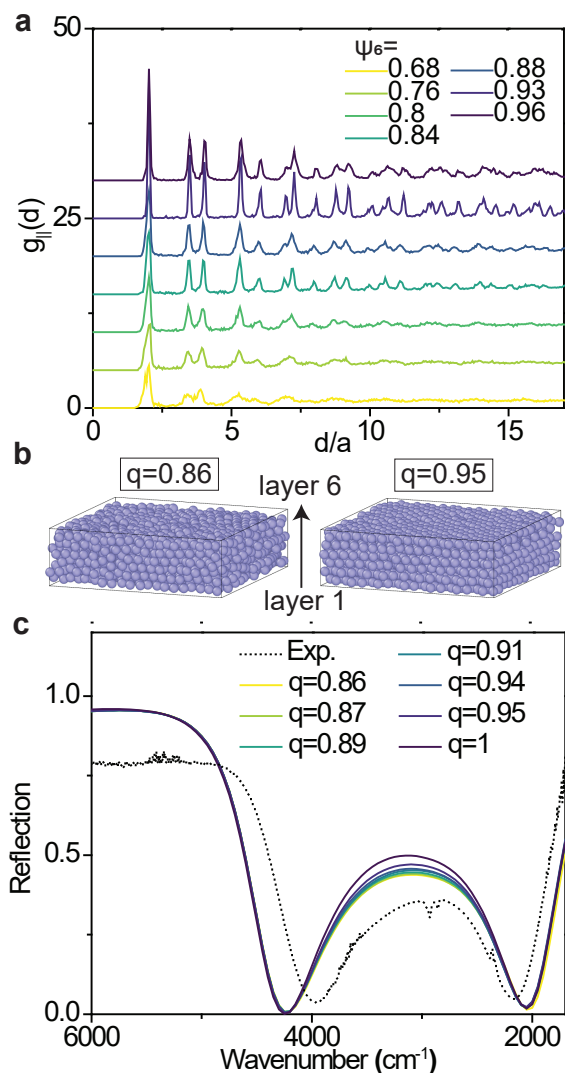
6

Figure 2: **Simulated disordered NC assemblies and their spectra in the Salisbury screen configuration.** (a) The in-plane pair distribution function ($g_{\parallel}(d)$) for NC monolayers with various values of the hexatic order parameter (ψ_6). (b) Two example configurations of six layers of disordered NCs with different relative Steinhardt bond-orientational order parameters (q). (c) Simulated reflection spectra as a function of q for six layers of 25 nm ITO NCs in a Salisbury screen configuration consisting of 160 nm Ge and 100 nm Au. The dashed line shows the experimental spectrum of a six-layer assembly of 25 nm 2.7% Sn ITO NCs in the Salisbury screen configuration.

7

simulations. Regardless of the disorder present, the linear increase in extinction with thickness, with little change in the spectral lineshape, suggests that the NC packing fraction remained relatively consistent. This characteristic could enable the computational design of more complex photonic structures with a thickness-independent effective optical response used to model the NC assembly as a metamaterial. To confirm this disorder tolerance, we used Brownian dynamics simulations (*41, 42*) to create a series of different six-layer NC assemblies. Each individual NC layer contained 361 particles for total of 2,166 NCs per configuration (see section 3.1 of SI for details and comparisons to a perfectly ordered lattice, Figure S3). The individual layers, while having the same final packing fraction, were pre-assembled using different nonequilibrium compression rates. This allowed us to vary the degree of structural disorder in each layer (*43*), quantified by the hexatic (two-dimensional) bond-orientational order parameter (ψ_6) (*29, 44*). The reduction in bond-orientational order for layers with lower ψ_6 was accompanied by a broadening of peaks in the pair distribution functions ($g_{\parallel}(d)$) which decay at progressively shorter pair separations, indicating a concomitant reduction of translational order (Figure 2a).

Next, we vertically stacked and compressed six layers of NCs, each with the same ψ_6, to create a disordered multilayer structure (Figure 2b). The disorder in these structures was quantified by the three-dimensional Steinhardt bond-orientational order parameter (q_6) and normalized as the relative q value, defined as $q_6/q_{6,\text{FCC}}$, where $q_{6,\text{FCC}}$ is the q_6 value for a perfectly ordered FCC lattice. As expected, we observed a positive correlation between q and ψ_6 in the stacked NC monolayers (Figure S4). The computed q values spanned the range accessible to multilayer sphere assemblies while holding the assembly NC volume fraction constant (*29, 43, 45*) (Figure S4). Observing the layer-dependent $g_{\parallel}(d)$ in the assembled six-layer stacks, we note that the disorder increases for NC layers further from the substrate (Figure S5). Our results are consistent with previous experimental observations in layered assemblies of micron-scale colloids that particle density is more broadly distributed and disorder increases with distance from the surface (*46*). In our case, the structural analysis demonstrates the successful creation of NC assemblies with varying levels of disorder.

Remarkably, the simulated optical spectra exhibited polariton modes with distinct UP and LP frequencies, characteristic of strong coupling, irrespective of the disorder present (Figure 2c). The reflection spectra were simulated for NC assemblies with varying q values (Figures 2b and S5) in a Salisbury screen configuration composed of 160 nm Ge and 100 nm Au. To calculate the

8

spectra, we used SMUTHI (Scattering by Multiple Particles in Thin-film Systems) (*47, 48*), an algorithm that combines T-matrix (transition-matrix) single-particle scattering computations with a scattering-matrix method to quantify the propagation of light through our layered structures (see section 3.2 of the SI for details). The experimentally determined electron concentrations and sizes of the NCs were used as inputs to the simulations and the NC volume fraction was fixed at a value that resulted in close agreement between the simulated CPR peak and that observed experimentally for a NC monolayer (Figure S6) (*31, 49*). Using these parameters to calculate the spectra of the cavity-coupled assemblies with variable disorder, we found that the reflection spectra are only slightly changed as q varied, with nearly invariant frequencies for the UP and LP and only slightly reduced reflection in the photonic stopband between the two dips for higher q. The spectra also well approximate the experimental reflection spectrum of a cavity-coupled six layer NC assembly, with $q = 0.86$ being the closest match (Figure 1d). These observations extend our previous results from large-scale simulations, which suggested that disorder has little effect on the extinction spectra of ITO NC monolayer superlattices (*29*). This defect tolerance contrasts with the development of plasmon polariton modes in thin slabs of gold NC superlattices, where precisely defined thicknesses of a few NC layers were required to locally establish F-P resonances that couple to the CPR of the superlattice medium, and disorder caused substantial broadening (*21, 50*). Our advantage is that the cavity resonance is largely established by the uniform film of Ge, so less precision is demanded in the structures of the NC metamaterial assemblies.

Modeling and Quantum Mechanical Analysis

Owing to the disorder-tolerant nature of the plasmon-polaritons, the spectra of the cavity-coupled NC assemblies can be accurately predicted by finding an effective optical response for the NC layer and using the transfer matrix model. We first fit the optical response of a NC monolayer using a slab of effective medium with a Lorentzian oscillator response, as established in our previous work (*28, 31*). The Lorentzian oscillator permittivity found by fitting the optical response of a NC monolayer closely recreates the extinction spectra for multilayers of NCs on silicon, as well, by simply scaling the thickness of the effective medium slab in the transfer matrix model framework according to the experimental number of NC layers (Figure S2). Likewise, the permittivity found by
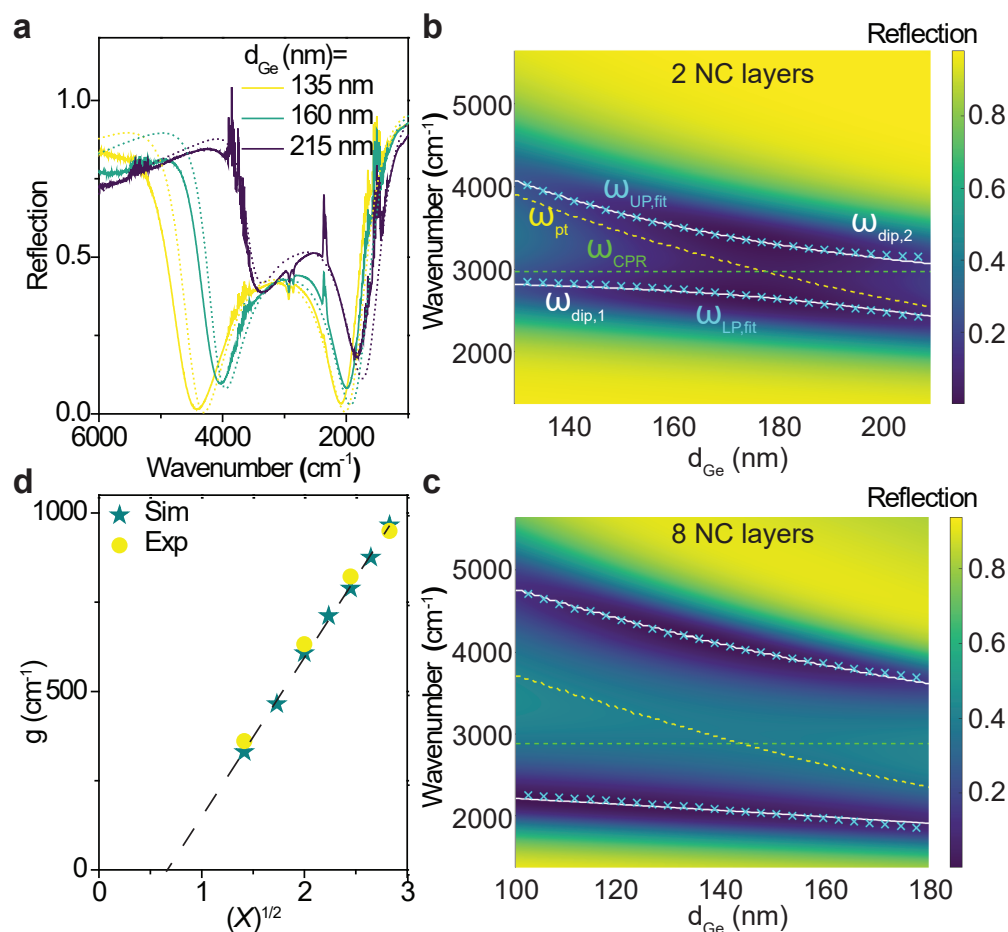
<div align="center">9</div>

Figure 3: **Analysis of the reflection spectra of multilayer NC assemblies in the Salisbury screen configuration.** (a) Reflection spectra of eight layers of 25 nm, 2.7% Sn ITO NCs in the Salisbury screen configuration with varying Ge thickness (d_{Ge}). The dotted lines show the simulated spectra using the transfer matrix method, where the NC assembly is treated as an effective medium. (b) Optical mode dependence on d_{Ge} for two NC layers, generated using the transfer matrix method. $\omega_{dip,1}$ and $\omega_{dip,2}$ correspond to two reflection minima, while $\omega_{UP,fit}$ and $\omega_{LP,fit}$ represent the frequencies based on the Hopfield Hamiltonian. (c) Optical modes for eight NC layers with varying d_{Ge}. (d) Coupling strength (g) extracted from experiments and fits from the transfer matrix simulations to the Hopfield Hamiltonian for variable number of NC layers (X). The square root of the number of NC layers is shown on the x-axis.

10

independently fitting to the extinction of multilayers of NCs varied little from the permittivity found for a monolayer, underscoring the consistency of the NC assembly structure and optical properties as layers are added. Also consistent with this finding, the effective permittivity found by explicitly calculating the optical response for a variable number of NC layers (using SMUTHI) (*51–54*) is also nearly invariant with layer number (Figure S2).

Using the effective NC layer permittivity together with the Ge and gold permittivities (*55*) (see section 4 in the SI), we model the integrated photonic structures in the transfer matrix framework (*56*) to obtain reflection spectra that accurately reproduce experimentally observed reflection dip positions, their intensities, and the overall spectral lineshapes, regardless of layer count or spacer layer thickness (Figure 3a and Figure S7). This simplified analytical approach using the transfer matrix method not only aids in understanding the origins of the optical features, but also helps to solve inverse problems for design of photonic structures incorporating ITO NC assemblies, including more complex assemblies incorporating layers of different NC compositions, which will be discussed in a later section.

Based on the accuracy of the effective medium and transfer matrix modeling in reproducing the experimental spectral lineshapes, we constructed reflection spectral maps that capture the dependence of the optical modes on spacer layer thickness (d_{Ge}) (Figure 3b, c, and S8). These correspond to dispersion relationships that describe the coupling behavior across different k-space values determined by the d_{Ge} within a quantum mechanical framework. The dispersion relations obtained from the angle dependence of the spectra do not show significant frequency shifts due to the high refractive index of Ge (Figure S9). Given the increasing and substantial peak splitting observed as additional NC layers are stacked, we hypothesized that the optical modes of polaritons might be well described by the Hopfield Hamiltonian (*8*),

$$H = \hbar\omega_{pt}\hat{a}^{\dagger}\hat{a} + \hbar\omega_{CPR}\hat{b}^{\dagger}\hat{b} + H_{int} + H_{A^2}. \tag{1}$$

Here, $\hbar = h/2\pi$, h is Planck's constant, and the interaction Hamiltonian, H_{int} depends on the coupling g and is defined as

$$H_{int} = \hbar g(\hat{a}^{\dagger} + \hat{a})(\hat{b}^{\dagger} + \hat{b}). \tag{2}$$

The diamagnetic Hamiltonian term, H_{A^2}, is given by

$$H_{A^2} = \hbar\frac{g^2}{\omega_{pt}}(\hat{a}^{\dagger} + \hat{a})^2. \tag{3}$$

11

This term describes how the induced polarization from the cavity-coupled material modifies the original photon field through a nonlinear feedback loop, particularly in the ultrastrong coupling regime.

Here, $\hat{a}^{\dagger}, \hat{a}, \hat{b}^{\dagger}, \hat{b}$ represent the creation and annihilation operators for photons and plasmon excitations, respectively, while ω_{pt} and ω_{CPR} denote the uncoupled photonic and CPR mode frequencies. The coupling strength, g, is defined as $\mu_{\text{CPR}}\sqrt{N}E_{\text{vac}}\omega_{\text{CPR}}/\omega_{\text{pt}}$, where μ_{CPR} is the CPR transition dipole moment, N is the number of NCs, and E_{vac} is the vacuum electric field per surface area. The vacuum electric field is expressed as $E_{\text{vac}} = \sqrt{\hbar\omega_{pt}/(2\varepsilon\varepsilon_0 A L_{\text{eff}})}$, with ε_0 and ε being the vacuum and relative permittivity in the photonic structure, respectively, A is the measurement surface area, and L_{eff} is the effective optical pathlength of the photonic structure. Assuming $L_{\text{eff}} = \lambda_{\text{pt}}/4n$, where n is the effective refractive index, which is equivalent to $\sqrt{\varepsilon}$, the coupling strength can be rewritten as $g = \mu_{\text{CPR}}\omega_{\text{CPR}}\sqrt{\hbar N/(\pi\varepsilon_0 ncA)}$. Note that N/A is the NC density per area, which is constant regardless of the measurement area and scales linearly with layer number. We treat n as a constant with varying d_{Ge}, and thus g is considered constant in the dispersion relationship for a given number of NC layers. Diagonalizing the Hamiltonian yields the polariton frequencies ω_{pp} as:

$$\omega_{\text{pp}}^{\pm} = \sqrt{\frac{\omega_{\text{pt}}^2 + 4g^2\omega_{\text{pt}}/\omega_{\text{CPR}} + \omega_{\text{CPR}}^2 \pm \sqrt{\left[\omega_{\text{pt}}^2 + 4g^2\omega_{\text{pt}}/\omega_{\text{CPR}} + \omega_{\text{CPR}}^2\right]^2 - 4\omega_{\text{pt}}^2\omega_{\text{CPR}}^2}}{2}} \quad (4)$$

where ω_{pp}^+ and ω_{pp}^- represent the upper ($\omega_{\text{UP,fit}}$) and lower ($\omega_{\text{LP,fit}}$) polariton frequencies, respectively.

Using this model, we fit the transfer matrix model-generated dispersion relations to the Hopfield Hamiltonian (Eq. 4), minimizing the difference between the observed ω_{dip} values and the fitted $\omega_{\text{UP,fit}}$ and $\omega_{\text{LP,fit}}$ values, while adjusting ω_{pt} and g as free parameters (Figure 3b and c). We fix the value of ω_{CPR} based on the peak position of the extinction spectrum of the NC assembly on silicon (Figure 1c). For two NC layers on the Ge spacer (Figure 3b), there was good agreement between the simulated reflection minima (solid white lines, ω_{dip}) and the fit to the model (blue x marks, $\omega_{\text{UP,fit}}$ and $\omega_{\text{LP,fit}}$). However, for thicker NC layers (Figure 3c), some discrepancies were observed: the Hopfield model slightly underestimates the frequency difference between the UP and LP for thinner d_{Ge} and overestimates the splitting for thicker d_{Ge}. We suspect that the simplifying assumptions made in deriving the Hamiltonian and defining g are responsible for these minor deviations. One

12

example is the assumed constant n value, which breaks down for thicker ITO NC films, since the NC layer itself, not only the Ge, contributes significantly to the optical path. Nonetheless, despite its approximate nature, this physics-based description of the coupled optical system is useful for examining trends in the coupling behavior.

The widening Rabi splitting of the polariton peaks with layer count suggests stronger coupling, which can be quantitatively assessed by examining the trend in the coupling strength g (Figure 3d). Even with a bilayer of NCs, the normalized coupling strength, g/ω_{CPR}, is 0.1 and the Rabi splitting at zero detuning ($2g$) is 20% of the CPR frequency (12), already meeting the ultrastrong coupling criterion. In addition, the coupling constant linearly increases with the square root of the number of NC layers (X), $\propto \sqrt{X}$, which agrees with previous studies of dipolar transition media in F-P cavities ($39, 57$). As a result, eight layers of NCs achieve $g/\omega_{\mathrm{CPR}} \approx 0.3$, demonstrating the possibility of controlling the g value simply by iterating NC stacking. However, we expect that the g value will eventually saturate for larger NC thickness as the portion of the optical path contributed by the NC layer becomes dominant, leading to a situation similar to NC-only cavity structures, where coupling was found to be approximately independent of NC layer thickness (20).

Designing Cavity-Coupled NC Assemblies to Target Spectral Windows

The spectral tunability of the cavity-coupled NC structures studied here, combined with the efficacy of the transfer matrix method in predicting their optical response, allows us to design assemblies that approximately realize targeted optical spectra. Of particular interest, the strong CPR-photonic mode coupling and the double-resonant spectral characteristic of the polariton modes suggest that we can design for applications requiring double-resonant absorption in the IR region. To illustrate this, we targeted an optical spectrum closely corresponding to the atmospheric transparency spectrum, which exhibits two main transparency windows (58), one between 770–$1250 \ \mathrm{cm}^{-1}$ (wavelengths of 8–$13 \ \mu\mathrm{m}$), and another between 2000–$3333 \ \mathrm{cm}^{-1}$ (wavelengths of 3–$5 \ \mu\mathrm{m}$), while largely blocking light at other frequencies. A significant challenge in this field is achieving independent control over visible light (either reflectance or transmittance, depending on the application) while absorbing and emitting strongly within the atmospheric transparency window (59), using a scalable materials approach (60). Given that our ITO NC synthesis and assembly processes are scalable, replacing Ge
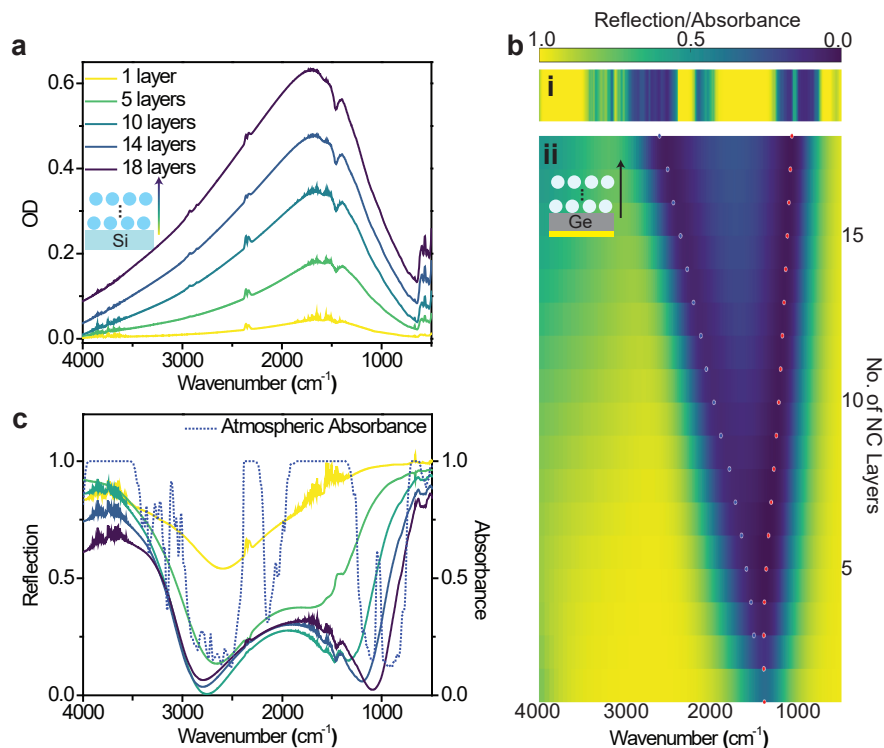
13

Figure 4: **Cavity-coupled NC assembly designed to target the atmospheric transparency windows.** (a) Extinction spectra of 0.6% 29 nm ITO NC films on IR-transparent Si wafers as a function of the number of NC layers. (b) (i) Atmospheric transparency window spectrum shown as absorbance (1-transmittance). (ii) Predicted reflection spectra of the same NCs from (a) in the Salisbury screen configuration as a function of the number of NC layers. The d_{Ge} thickness was optimized for each NC layer count to maintain consistent effective optical thickness. Matching the reflection dips of the photonic-NC assembly with the atmospheric absorbance minima maximizes thermal emission through Earth's atmosphere. (c) Experimental reflection spectra of NCs from (a) on a 205 nm Ge spacer and gold layer for various NC layer counts. The configuration with 18 NC layers exhibits excellent overlap with the atmospheric transparency spectrum, shown as absorbance.

14

with a visible light-transparent spacer could meet these requirements, making our cavity-coupled NC assemblies applicable for large-area radiative cooling applications. Assemblies of ITO NCs can have their CPR resonance in this range, *e.g.*, an assembly of 29 nm ITO NCs with 0.6% Sn doping has a CPR peak around 1690 cm^{-1} regardless of the number of NC layers. But, this single resonance peak cannot approximate the dual-band atmospheric transparency spectrum, even if the peak frequency is optimized by adjusting the Sn doping concentration. Furthermore, the optical extinction per layer of NCs in assemblies with such low Sn concentrations is weak due to the low electron concentration (Figure 4a and S10), so very thick NC layers would be needed to achieve near-perfect emissivity (perfect absorption), even at the wavelength corresponding to the CPR peak (*61*).

However, when these 0.6% Sn ITO NCs are incorporated in the Salisbury screen configuration, spectral tunability towards the atmospheric spectrum is achieved, as coupling gives rise to strong reflection dips (absorption peaks) in two distinct frequency regions. By assuming a consistent effective permittivity for the low-doped ITO NC assembly as NC layer count is varied, we modeled the reflection spectrum of the coupled architecture using the transfer matrix method. To maintain a resonance condition for the photonic mode and NC CPR, we adjusted the d_{Ge} to a lower value as the NC layer thickness increased (see section 5 of the SI for details). While thinner NC assemblies exhibit a single reflection dip around the original CPR frequency, thicker NC layers exhibit significant peak splitting in the reflection spectra. For instance, 18 NC layers show the LP around 1100 cm^{-1} and the UP around 2750 cm^{-1} [Figure 4b (ii)]. This pronounced peak splitting creates a dual-mode spectrum that aligns well with the two bands in the atmospheric transparency spectrum [Figure 4b (i)].

Implementing this design, our experimental results confirm that 18 layers of NCs in a Salisbury screen configuration with $d_{\text{Ge}} = 205$ nm produce strong absorption at frequencies corresponding to the two atmospheric transparency windows, demonstrating the potential of such assembled photonic architectures for radiative cooling applications (Figure 4c and S10). By leveraging the high degree of design flexibility, from NC synthesis to Salisbury screen configuration tuning, we can significantly improve the atmospheric spectral matching compared to single-mode emissive coatings while using the active material much more efficiently since the layer thickness needed to achieve perfect absorption is reduced greatly by photonic coupling (*31, 61*).

15

Understanding the Optical Modes with Near-Field Probes

To understand how the plasmon polariton modes may be used for applications such as nonlinear optics (*62*) and molecular sensing (*63*), it is crucial to understand the spatial distribution of the electric field. While NC monolayers in a Salisbury screen can be conceptualized in the ultrathin-absorber limit (*31, 64*), we expect that the phase shift of the electric field within the thicker NC assemblies considered here can be significant. To assess the spatial variation of the electric near-field along the out-of-plane (*z*)-dimension, we employed NC surface-bound molecules as vibrational spectroscopic probes. Our previous study on NC monolayers demonstrated that the molecular vibration signal on the surface of the NCs serves as an effective experimental probe for evaluating the enhancement of the electric field in the gaps between NCs (*35*). Although the local near-field intensities can be determined for idealized assemblies by finite element simulations (FEM), using molecular vibrational signals as an experimental probe (*65, 66*) can help reveal the nature of the optical modes in the real, structurally complex cavity-coupled NC assemblies. Our previous results on NC monolayers established a correspondence between plasmon-enhanced vibrational signal intensity and the surface-averaged electric field predicted by electromagnetic simulations (*35*), thus validating this approach.

To probe the spatial variation of the local electric field at the frequency of characteristic molecular vibrations, we fabricated NC assemblies where a single, select layer of NCs contains molecular probes. 4-Azidobenzoate (ABA) was used as the molecular probe on the NC surface, with its azide stretching vibration serving as a strong and quantifiable electric field indicator. For NC layers without the molecular probe, oleyl phosphate (OP)-capped ITO NCs were used to protect the NC surface and prevent unintended ligand exchange with ABA since the phosphorate head group binds more strongly to the NC surface than the ABA carboxylate group. We verified that OP-passivated NCs do not undergo ligand exchange with ABA upon dipping into an ABA-containing solution, as the azide molecular vibration signal was absent afterward (Figure S11). Hence, the ABA was exclusively present on specific NC layers where we intended to assess the local electric field strength.

We assembled five layers of 25 nm, 2.7% Sn-doped ITO NCs, with ABA selectively introduced in specific layers of the NC assembly, atop a 160 nm thick Ge spacer layer (Figure 5a). Regardless
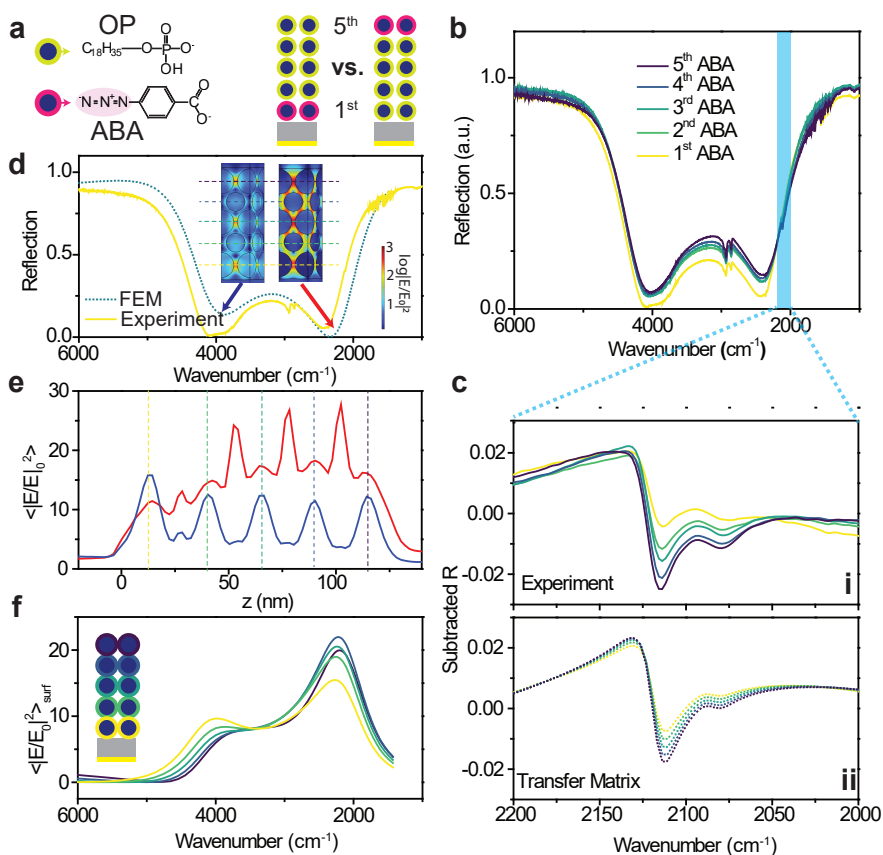
Figure 5: **Mapping the near-field with vibrational probe molecules.** (a) Schematic representation of ITO NCs capped with oleyl phosphate (OP) or azidobenzoate (ABA). NC layer stacks are assembled with ABA-capped NCs in one selected layer, with the rest capped by OP, to probe the layer-dependent electric field intensity. (b) Far-field extinction spectra of five layers of 2.7% Sn ITO NCs, 25 nm in diameter, on a 160 nm Ge spacer layer and gold backing. The layer containing NCs capped with ABA molecules is indicated in the legend. (c) (i) Magnified molecular vibration region of the spectra after subtracting the plasmon-photon coupled lineshape. (ii) Transfer matrix model-predicted molecular vibration intensity trend, which reproduces the experimental trends accurately. (d) Overlaid experimental and finite element method (FEM)-predicted far-field spectra. The electric field distribution at each dip is also shown. (e) Averaged electric field along the z-dimension for the ITO NC stack at the LP and UP frequencies. The frequency of the probed electric field and the dashed lines correspond to the LP and UP features and the z positions shown in (d). (f) NC surface-averaged electric field intensity ($\langle |E/E_0|^2 \rangle_{surf}$) spectrum within each NC layer, color coded as shown in the schematic.

17

of the position of the molecular vibration, the overall lineshape of the reflection spectra remained unchanged (Figure 5b). A distinct molecular vibration feature appeared around $2100\,\mathrm{cm}^{-1}$, slightly red-shifted relative to the LP feature of the photonic structure. We observed that the molecular vibration intensity increases two-fold when ABA molecules are located in the NC layer farthest from the Ge spacer compared to the intensity when they are located in the bottom layer of NCs. This trend becomes more apparent when the plasmon-photon background is subtracted [Figure 5c (i)]. The vibrational probe thus indicates a stronger electric field intensity nearer the top surface of the assembly. In contrast, the vibrational signal strength increased by only about 30% for the ABA-functionalized layer farthest from the substrate in ITO NC assemblies fabricated on IR-transparent Si substrates, while the probe signal was independent of which layer was functionalized for non-plasmonic In_2O_3 NCs assembled in the Salisbury screen configuration (Figure S12). Thus, the coupled CPR-cavity modes experience a more pronounced electric field intensity variation along the z-axis than the CPR or cavity modes alone.

The intensity trend of the molecular vibration probe was reproducible by modeling the permittivity function of a NC monolayer containing molecular vibrations using coupled mode theory (details in section 6 of the SI) (*21, 23*). By incorporating this vibration-coupled permittivity function for the select layer in the assembly (Figure S13 and S14), we observed the same vibration intensity trend as in the experiments, where the intensity increases when the probe molecules are located on the NC layers farther from the substrate [Figure 5c (ii) and S14]. In addition, this permittivity function captures the molecular vibration intensity trends in NC asemblies both with [Figure 5c (ii)] and without cavity coupling (Figure S12), where the vibration intensity becomes three times greater in the Salisbury screen than in the transmission signal of an equivalent assembly on a silicon substrate. Therefore, the near-field enhancement profile control is a collective effect resulting from the coupling between the CPR and the photon mode facilitated by the Salisbury screen configuration.

To understand the origin of the spatially varying vibration probe signal, we used FEM to evaluate the near-field distribution with explicit NC layers. We modeled five layers of 25 nm ITO NCs, which produces a simulated extinction spectrum similar in optical density and linewidth to that of a corresponding experimental sample consisting of five layers of 2.7% Sn, 25 nm ITO NCs on a Si wafer (Figure S15). By placing this assembly on a 160 nm Ge spacer and 100 nm Au reflector, we simulated a similar far-field reflection spectrum as observed experimentally, with two

polariton modes appearing as reflection dips (Figure 5d). Examining the electric field distributions, we find that excitation at the LP frequency leads to electric field confinement on the NC surfaces, while exciting at the UP results in a more delocalized electric field, both outside and inside the NCs. The z-dependence of the field distribution also appears to differ between the two polariton modes, which we quantified by calculating the average electric field intensity vs z (Figure 5e). At the LP, intense peaks are observed *between* the NC layers, as well as at z values corresponding to the NC centers. This concentration of the field within both intralayer and interlayer gaps holds great promise for enhancing transitions of optical components that may be embedded within the NC assembly. Indeed, the strong vibration signal enhancement of the ABA molecules, whose azide stretching frequency is closer to the LP than to the UP, is consistent with this finding. In addition, under excitation at the LP, the electric field intensity within the NC layers grows with increasing distance from the substrate, with only a slight decrease at the last layer. In contrast, the bottom-most layer has the strongest electric field intensity at the UP frequency.

To better connect the electric field intensity trends to the molecular vibration intensities observed in our experiments, we analyzed the surface-averaged electric field ($\langle|E/E_0|^2\rangle_{\text{surf}}$) for each NC layer (Figure 5f) based on the FEM simulations. We found that the electric field becomes stronger at the LP (2200 cm^{-1}) for upper NC layers, while it weakens slightly for upper layers under excitation at the UP frequency. In a NC assembly on a silicon wafer, conversely, FEM simulations show that the $\langle|E/E_0|^2\rangle_{\text{surf}}$ at the frequency corresponding to the vibrational mode does not significantly depend on the layer probed (Figure S15). The possibility of controlling the near-field enhancement along the z-dimension can provide a new tuning knob for selectively intensifying or weakening the electric field at certain locations for distinct resonant frequencies. This type of control may be useful for non-linear optical processes (*67*) or sensing purposes (*68*), which rely on frequency-specific operations.

Engineering the Spatial Concentration of Light with Multicomponent NC Assemblies

To deliberately sculpt the spatial distribution of the optical modes and achieve distinct far-field spectral characteristics, we explored stacking different types of ITO NCs to make a multi-resonant
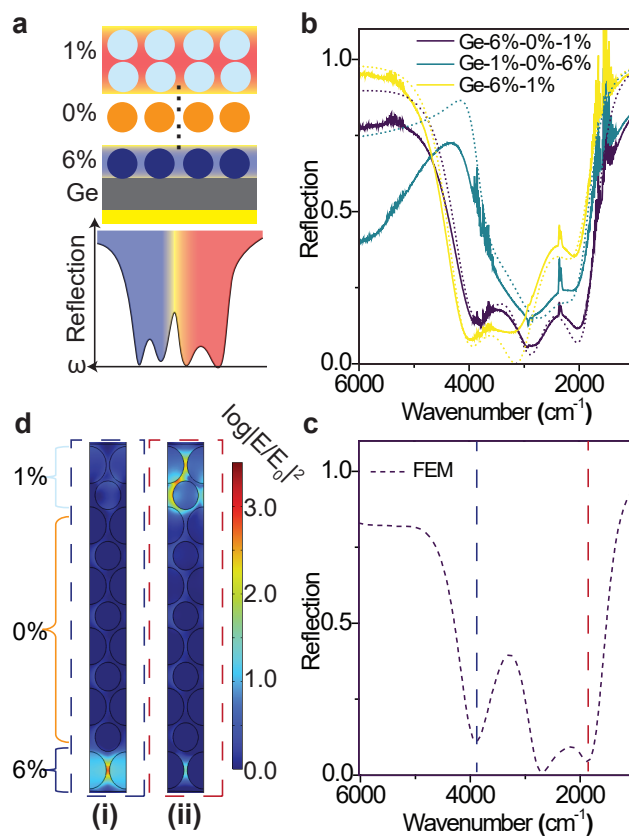
19

Figure 6: **Cavity structure with multiple resonances by stacking different types of NCs** (a) Schematic representation of a photonic structure composed of a monolayer of highly doped (6% Sn) ITO NCs, multilayers of undoped (0%) In_2O_3 NCs, and two layers of low-doped (1% Sn) ITO NCs on a Ge spacer layer. Multiple resonances are expected to appear in the reflection spectrum, with distinct spatial localizations. (b) Far-field reflection spectra of cavity-coupled NC assemblies with various stacking sequences. The legend indicates the stacking sequence combinations of 6% Sn ITO, 1% Sn ITO, and In_2O_3 NCs. The dotted lines represent the reflection spectra predicted using the transfer matrix model. (c) Far-field reflection spectrum predicted using FEM for the Ge-6%-0%-1% case. (d) Near-field intensity distributions corresponding to the same configuration as in (c) for excitation at high and low resonance frequencies indicated by the dashed lines in (c).

20

photonic structure (Figure 6a and Figure S16). Based on the principle of the Salisbury screen configuration, which requires a spacer layer approximately a quarter wavelength thick to achieve resonance with the absorbing layer, we design the Salisbury screen configuration with highly Sn-doped 31 nm NCs (6% Sn) on a relatively thin Ge spacer layer. Then, we added another dielectric spacer by stacking 11 layers of undoped indium oxide (In_2O_3) NCs (25 nm in diameter), which are transparent at IR frequencies due to negligible plasmonic response. Finally, we topped the assembly with a bilayer of low Sn-doped 31 nm NCs (1% Sn), where the spacing between the low-doped NCs and the gold layer is significantly augmented by the many intervening NC layers. Therefore, this structure offers the possibility of two independently tuned modes within a single photonic structure, where each photonic mode can couple resonantly to NCs with different doping concentrations.

Indeed, the reflection spectrum of this structure shows a very broad absorption feature, which can be ascribed to a double resonance effect at high and low frequencies (Figure 6b). The lineshape is also well reproduced by the transfer matrix method by modeling the NC stack as three different effective medium slabs atop the germanium and gold layers (details are in section 8 of the SI). In addition, we highlight that the sequence of NC stacking is important for maximizing the broad absorption: reversing the stacking order of the 1% and 6% Sn ITO NC layers or omitting the In_2O_3 NC spacer layer between them does not produce a lineshape as broad as what we observed with the correct, as-designed stacking order (Figure 6b).

We can also reproduce a similar lineshape with FEM (Figure 6c) by stacking same-sized NCs but with different electron concentrations, mimicking the experimental dual resonant structure. Note that we only stack eight layers of 30 nm In_2O_3 NCs, which substitutes for the 11 layers of 25 nm In_2O_3 NCs used in our experiments. We analyzed the electric field maps for different incident frequencies, where we observed strong activation of the lower-layer, highly doped ITO NCs, at high incident light frequency ($\omega = 3850$ cm^{-1}, Figure 6d). In contrast, at low frequency ($\omega = 1800$ cm^{-1}), the upper part of the photonic structure showed strong electric field intensity, although a small contribution from the highly doped NCs was still evident (Figure 6d). This behavior is also reflected in the z-dependent electric field intensity, where strong localization of light of each frequency is observed (Figure S17).

With this spatially selective concentration of the electric field depending on the optical frequency, we can envision creating assemblies useful for cooperative functionality between different

21

layers. The strongly confined electric fields (Figure 6d) could induce nonlinear optical behavior useful for noise filtering (*69*) or logic gates (*70*). In addition, we expect the combinatorial effect of spatial control for both phase matching (*71, 72*) and frequency matching (*73*) to significantly enhance harmonic generation efficiency. Therefore, we expect that future developments could enable these NC-integrated photonic structures to find use for photonic technologies.

Discussion

We demonstrated a cavity structure that allows easy integration of widely tunable NC assemblies to achieve diverse optical resonance frequencies, lineshapes, and spatial modes through systematic variation of the NC stack composition. By observing the frequency splitting as the number of NC layers increased, we demonstrated that ultrastrong coupling occurs for thicker ITO NC assemblies. Compared to other approaches for achieving plasmon polaritons, this architecture is amenable to easy fabrication and produces a consistent optical response over large areas, despite the structural disorder of the NC assemblies due to the defect-tolerant nature of the optical modes. The key conceptual advance is that the cavity resonance is established primarily by the uniform blanket deposition of metal and dielectric spacer layers, not relying on lithography or a precise organization of the NCs in a superlattice or array to establish the photonic mode. The resulting strong peak splitting at IR frequencies could be used to design optical response for applications such as radiative cooling, by matching the absorption to the atmospheric transparency spectrum. This cavity structure enables spatially guiding the electric field intensity within the NC assembly, where molecular vibrations serve as near-field intensity probes, revealing that low-frequency light exhibits the strongest electric field within the NC gaps in the topmost layer. Finally, by stacking NCs with different doping concentrations, we can confine light of different frequencies at varying heights within the assembly. Such spatial control over the modes could be leveraged in the future for photonic application.

With this foundational understanding and the configuration of the photonic architecture as an 'open' cavity, these structures could be further accessorized by incorporating photoactive molecules or quantum dots within the intense electric field hot spots produced in the NC gaps (*74–76*). Such multiplexed architectures could achieve a wide range of photonic conversion processes, such as

fusion (*77*) or fission of excitons (*78*) to upconvert or downconvert the frequency of incident light. Alternatively, coupling to vibrational modes of embedded molecules might be used to manipulate their chemical reactivity and guide reaction selectivity (*79*). The open cavity architecture, with consistent optical modes across a large area, provides opportunities for flow-through sensors or reactors and simplifies integration with optical circuits. In addition, electrochemical modulation of the electron concentration within the NCs (*80, 81*) or the thickness of the dielectric layer (*82*) could enable dynamically tunable resonance modes. Overall, the extensive tunability of the NC-photonic platform introduced here is ripe for creative exploitation.

Materials and Methods

Materials

All chemicals were used as received, without any additional purification. Indium (III) acetate [$In(ac)_3$, 99.99%, Sigma Aldrich], tin (IV) acetate [$Sn(ac)_4$, Sigma Aldrich], oleic acid (OA, 90%, technical grade, Sigma Aldrich), oleyl alcohol (OLA, 90%, technical grade, Sigma Aldrich), and octadecene (ODE, 85%, technical grade) were used to synthesize the NCs. Hexane ($\geq$99.9%, Fischer Chemical), tetrachloroethylene ($\geq$99.5%, Sigma Aldrich), and acetonitrile (Fisher Scientific, 99%) were used for the dispersing NCs to form the assemblies. Oleyl phosphate (OP, TCI America, Mono- and Di- Ester mixture) and 4-azidobenzoic acid (ABA, TCI America, $\geq$97%) were used for exchanging ligands on the NC surfaces.

Synthesis of ITO NCs

NCs were synthesized by slow injection methods based on previous reports (*28, 32*). For ITO NCs around 30 nm, we dissolved $8 \times (1\text{-}x)$ mmol of $In(ac)_3$ and $8 \times x$ mmol of $Sn(ac)_4$ in 16 mL of OA and 8 mL of ODE. x is determined by the desired doping concentration, where 1% and 6% ITO NC correspond to x=0.01 and x=0.06, respectively. We heated this solution to 150 °C under a nitrogen atmosphere for two hours. In a separate flask, 13 mL of OLA was degassed under vacuum for one hour at 120 °C. Then, the OLA flask was heated to 290 °C under nitrogen flow. We injected 21 mL of the precursor solution into the OLA with an injection rate of 0.3 mL min^{-1} using a syringe

<div align="center">23</div>

pump. Once the injection was complete, we waited for an extra 20 min at 290 °C and cooled the flask naturally until it reached room temperature. We washed the product with ethanol three times and redispersed it in 10 mL of hexane.

For 25 nm ITO NCs, we dissolved 0.5×0.973 mol L^{-1} of In(ac)$_3$ and 0.5×0.027 mol L^{-1} of Sn(ac)$_4$ in OA and degassed the solution under vacuum for one hour at 100 °C. We then heated this precursor up to 150 °C for 2 hours under nitrogen. We separately prepared 13 mL of OLA under nitrogen at 290 °C, then slowly injected 25 mL of the precursor solution at 0.35 mL min^{-1} at 290 °C using a syringe pump. For this injection, we first inject 10 mL of precursor, then stop the injection and start the injection of 10 mL OLA at a rate of 0.2 mL min^{-1}. We repeated OLA injection step one more time after we added an additional 10 mL of metal precursor. Synthesized NCs are centrifuged with an excess amount of ethanol after diluting the NC dispersions with hexane. The washed NCs are redispersed in hexane.

ITO NC Characterization

Synthesized ITO NCs and monolayers of ITO NCs were imaged using a Hitachi S5500 scanning transmission electron microscope (STEM) under the bright field STEM and secondary electron (SE) modes, respectively. For inductively coupled plasma mass spectrometry (ICP-MS), we first dried the ITO NC solution and added aqua regia for digestion. After two days of digestion, we diluted this solution to 2% nitric acid and utilized an Agilent 7500ce spectrometer to measure the concentration of each element. The sizes of the synthesized ITO NCs were analyzed by small-angle X-ray scattering (SAXS) using an in-house SAXSLab Ganesha.

Photonic Structure Fabrication

We sequentially deposited a 5 nm titanium (Ti) adhesion layer, 100 nm of Au, and variable Ge dielectric spacer by e-beam evaporation (PVD 75 from Kurt J Lesker) onto silicon substrates. The ITO NC monolayer preparation was carried out as described in our previous work (*35*). We dropped NC solution (dispersed in hexane, 3 mg mL^{-1}) onto 5 mL of acetonitrile solution in a Teflon trough, where the monolayer of ITO NC is formed within 30 seconds. After draining the acetonitrile subphase, the monolayer NC film was transferred onto the substrate, which was immersed in the

24

acetonitrile in advance of NC deposition. We iterate this procedure to make a multilayer of ITO NCs. For extinction spectra measurements of NC assemblies, we did the same procedure on double-side polished undoped silicon wafers. For ligand exchange with ABA, the acetonitrile solution contains 10 mM of ABA solution. And once the NC monolayer is formed, we wait for 30 minutes to ensure the ligand exchange before transferring the monolayer to the substrate. OP ligand exchange was done colloidally where we disperse 10 mg of NC in 1 mL of $CHCl_3$ containing 10 mM of OP. After stirring overnight, we washed the NCs with hexane and ethanol three times and resuspended in pure hexane at 3 mg mL^{-1} concentration. We used OP capped NC for making monolayers in the same manner as NCs capped with native oleate ligands.

Optical Measurements

The extinction spectra of the NCs on double-side polished Si wafers were measured with a Bruker Vertex 70 Fourier transform infrared (FT-IR) spectrometer in the transmission configuration with a 1 cm beam diameter holder. For reflection spectra of cavities, we used a specular reflection accessory (Pike Industries 10 Spec). For angle-dependent measurements, we used a VeeMax III from Pike Industries. For all reflection spectroscopy measurements, a gold-coated substrate, providing near-perfect reflection in the mid-IR, served as a reference.

References

1. H. Gibbs, G. Khitrova, S. Koch, Exciton–polariton light–semiconductor coupling effects. *Nat. Photonics* **5**, 273–273 (2011).

2. T. W. Ebbesen, Hybrid light–matter states in a molecular and material science perspective. *Acc. Chem. Res.* **49**, 2403–2412 (2016).

3. A. Imamog, R. Ram, S. Pau, Y. Yamamoto, Nonequilibrium condensates and lasers without inversion: Exciton-polariton lasers. *Phys. Rev. A* **53**, 4250 (1996).

4. S. Joseph, S. Sarkar, J. Joseph, Grating-coupled surface plasmon-polariton sensing at a flat metal–analyte interface in a hybrid-configuration. *ACS Appl. Mater. Interfaces* **12**, 46519–46529 (2020).

5. C. Zhao, W. Xu, L. Li, C. Zhang, F. Peeters, Terahertz plasmon-polariton modes in graphene driven by electric field inside a Fabry-Pérot cavity. *J. Appl. Phys.* **117** (2015).

6. K. Bhattarai, Z. Ku, S. Silva, J. Jeon, J. O. Kim, S. J. Lee, A. Urbas, J. Zhou, A large-area, mushroom-capped plasmonic perfect absorber: Refractive index sensing and Fabry–Perot cavity mechanism. *Adv. Opt. Mater.* **3**, 1779–1786 (2015).

7. B. Cohn, K. Das, A. Basu, L. Chuntonov, Infrared open cavities for strong vibrational coupling. *J. Phys. Chem. Lett.* **12**, 7060–7066 (2021).

8. D. G. Baranov, B. Munkhbat, E. Zhukova, A. Bisht, A. Canales, B. Rousseaux, G. Johansson, T. J. Antosiewicz, T. Shegai, Ultrastrong coupling between nanoparticle plasmons and cavity photons at ambient conditions. *Nat. Commun.* **11**, 2715 (2020).

9. M. Hertzog, M. Wang, J. Mony, K. Börjesson, Strong light–matter interactions: a new direction within chemistry. *Chem. Soc. Rev.* **48**, 937–961 (2019).

10. J. Chen, Q. Zhang, C. Peng, C. Tang, X. Shen, L. Deng, G.-S. Park, Optical cavity-enhanced localized surface plasmon resonance for high-quality sensing. *IEEE Photonics Technol. Lett.* **30**, 728–731 (2018).

11. A. Konrad, A. M. Kern, M. Brecht, A. J. Meixner, Strong and coherent coupling of a plasmonic nanoparticle to a subwavelength Fabry–Pérot resonator. *Nano Lett.* **15**, 4423–4428 (2015).

12. A. Frisk Kockum, A. Miranowicz, S. De Liberato, S. Savasta, F. Nori, Ultrastrong coupling between light and matter. *Nat. Rev. Phys.* **1**, 19–40 (2019).

13. X. Shi, K. Ueno, T. Oshikiri, Q. Sun, K. Sasaki, H. Misawa, Enhanced water splitting under modal strong coupling conditions. *Nat. Nanotechnol.* **13** (10), 953–958 (2018).

14. Y. Suganami, T. Oshikiri, X. Shi, H. Misawa, Water oxidation under modal ultrastrong coupling conditions using gold/silver alloy nanoparticles and Fabry–Pérot nanocavities. *Angew. Chem.* **133**, 18586–18590 (2021).

15. C. Hägglund, G. Zeltzer, R. Ruiz, A. Wangperawong, K. E. Roelofs, S. F. Bent, Strong coupling of plasmon and nanocavity modes for dual-band, near-perfect absorbers and ultrathin photovoltaics. *ACS Photonics* **3**, 456–463 (2016).

16. E. Sánchez-Burillo, D. Zueco, J. Garcia-Ripoll, L. Martin-Moreno, Scattering in the ultrastrong regime: nonlinear optics with one photon. *Phys. Rev. Lett.* **113**, 263604 (2014).

17. P. Genevet, J.-P. Tetienne, E. Gatzogiannis, R. Blanchard, M. A. Kats, M. O. Scully, F. Capasso, Large enhancement of nonlinear optical phenomena by plasmonic nanocavity gratings. *Nano Lett.* **10**, 4880–4883 (2010).

18. L. A. Martínez-Martínez, R. F. Ribeiro, J. Campos-González-Angulo, J. Yuen-Zhou, Can ultrastrong coupling change ground-state chemical reactions? *ACS Photonics* **5**, 167–176 (2018).

19. E. B. Barros, B. G. Vieira, N. S. Mueller, S. Reich, Plasmon polaritons in nanoparticle supercrystals: Microscopic quantum theory beyond the dipole approximation. *Phys. Rev. B* **104**, 035403 (2021).

20. N. S. Mueller, Y. Okamura, B. G. Vieira, S. Juergensen, H. Lange, E. B. Barros, F. Schulz, S. Reich, Deep strong light–matter coupling in plasmonic nanoparticle crystals. *Nature* **583**, 780–784 (2020).

21. R. Arul, D.-B. Grys, R. Chikkaraddy, N. S. Mueller, A. Xomalis, E. Miele, T. G. Euser, J. J. Baumberg, Giant mid-IR resonant coupling to molecular vibrations in sub-nm gaps of plasmonic multilayer metafilms. *Light Sci. Appl.* **11**, 281 (2022).

22. D. J. Park, C. Zhang, J. C. Ku, Y. Zhou, G. C. Schatz, C. A. Mirkin, Plasmonic photonic crystals realized through DNA-programmable assembly. *Proc. Natl. Acad. Sci. U. S. A.* **112**, 977–981 (2015).

27

23. N. S. Mueller, E. Pfitzner, Y. Okamura, G. Gordeev, P. Kusch, H. Lange, J. Heberle, F. Schulz, S. Reich, Surface-Enhanced Raman Scattering and Surface-Enhanced Infrared Absorption by Plasmon Polaritons in Three-Dimensional Nanoparticle Supercrystals. *ACS Nano* **15**, 5523–5533 (2021).

24. M. Hertzog, B. Munkhbat, D. Baranov, T. Shegai, K. Borjesson, Enhancing vibrational light–matter coupling strength beyond the molecular concentration limit using plasmonic arrays. *Nano Lett.* **21**, 1320–1326 (2021).

25. M. Lafitte, R. Dwivedi, R. Elancheliyan, F. Lagugné-Labarthet, L. Buisson, I. Ly, P. Barois, A. Baron, O. Mondain-Monval, V. Ponsinet, Colloidal self-assembly of silver nanoparticle clusters for optical metasurfaces. *Langmuir* **40**, 2601–2615 (2024).

26. B. G. M. Vieira, N. S. Mueller, E. B. Barros, S. Reich, Plasmonic Properties of Close-Packed Metallic Nanoparticle Mono- and Bilayers. *J. Phys. Chem. C* **123**, 17951–17960 (2019).

27. C. M. Staller, S. L. Gibbs, C. A. S. Cabezas, D. J. Milliron, Quantitative Analysis of Extinction Coefficients of Tin-Doped Indium Oxide Nanocrystal Ensembles. *Nano Lett.* **19**, 8149–8154 (2019).

28. K. Kim, Z. M. Sherman, A. Cleri, W. J. Chang, J.-P. Maria, T. M. Truskett, D. J. Milliron, Hierarchically Doped Plasmonic Nanocrystal Metamaterials. *Nano Lett.* **23**, 7633–7641 (2023).

29. A. M. Green, W. J. Chang, Z. M. Sherman, Z. Sakotic, K. Kim, D. Wasserman, D. J. Milliron, T. M. Truskett, Structural order and plasmonic response of nanoparticle monolayers. *ACS Photonics* **11**, 1280–1292 (2024).

30. Z. M. Sherman, K. Kim, J. Kang, B. J. Roman, H. S. N. Crory, D. L. Conrad, S. A. Valenzuela, E. Lin, M. N. Dominguez, S. L. Gibbs, E. V. Anslyn, D. J. Milliron, T. M. Truskett, Plasmonic Response of Complex Nanoparticle Assemblies. *Nano Lett.* **23**, 3030–3037 (2023).

31. W. J. Chang, Z. Sakotic, A. Ware, A. M. Green, B. J. Roman, K. Kim, T. M. Truskett, D. Wasserman, D. J. Milliron, Wavelength tunable infrared perfect absorption in plasmonic nanocrystal monolayers. *ACS Nano* **18**, 972–982 (2024).

32. A. W. Jansons, J. E. Hutchison, Continuous Growth of Metal Oxide Nanocrystals: Enhanced Control of Nanocrystal Size and Radial Dopant Distribution. *ACS Nano* **10**, 6942–6951 (2016).

33. A. Dong, J. Chen, P. M. Vora, J. M. Kikkawa, C. B. Murray, Binary nanocrystal superlattice membranes self-assembled at the liquid–air interface. *Nature* **466** (7305), 474–477 (2010).

34. A. Dong, Y. Jiao, D. J. Milliron, Electronically coupled nanocrystal superlattice films by in situ ligand exchange at the liquid–air interface. *ACS Nano* **7**, 10978–10984 (2013).

35. W. J. Chang, B. J. Roman, A. M. Green, T. M. Truskett, D. J. Milliron, Surface-Enhanced Infrared Absorption Spectroscopy by Resonant Vibrational Coupling with Plasmonic Metal Oxide Nanocrystals. *ACS Nano* **18**, 20636–20647 (2024).

36. O. Erdem, S. Foroutan, N. Gheshlaghi, B. Guzelturk, Y. Altintas, H. V. Demir, Thickness-tunable self-assembled colloidal nanoplatelet films enable ultrathin optical gain media. *Nano Lett.* **20**, 6459–6465 (2020).

37. M. W. Berry, A. M. Green, B. J. Roman, T. M. Truskett, D. J. Milliron, Incorporating dopant effects in the plasmon ruler for metal-oxide nanocrystal superlattices. *ACS Mater. Lett.* **6**, 1929–1937 (2024).

38. J. M. Winkler, F. T. Rabouw, A. A. Rossinelli, S. V. Jayanti, K. M. McPeak, D. K. Kim, B. Le Feber, F. Prins, D. J. Norris, Room-temperature strong coupling of CdSe nanoplatelets and plasmonic hole arrays. *Nano Lett.* **19**, 108–115 (2018).

39. W. J. Chang, H. Zeng, C. K. Terry Weatherly, J. Provazza, P. Liu, E. A. Weiss, N. P. Stern, R. Tempelaar, Dark state concentration dependent emission and dynamics of cdse nanoplatelet exciton-polaritons. *ACS Nano* **18**, 20226–20235 (2024).

40. A. Jaber, M. Reitz, A. Singh, A. Maleki, Y. Xin, B. T. Sullivan, K. Dolgaleva, R. W. Boyd, C. Genes, J.-M. Ménard, Hybrid architectures for terahertz molecular polaritonics. *Nat. Commun.* **15**, 4427 (2024).

41. J. A. Anderson, J. Glaser, S. C. Glotzer, HOOMD-blue: A Python package for high-performance molecular dynamics and hard particle Monte Carlo simulations. *Comput. Mater. Sci.* **173**, 109363 (2020).

42. D. Heyes, J. Melrose, Brownian dynamics simulations of model hard-sphere suspensions. *J. Nonnewton. Fluid Mech.* **46**, 1–28 (1993).

43. T. M. Truskett, S. Torquato, P. G. Debenedetti, Towards a quantification of disorder in materials: Distinguishing equilibrium and glassy sphere packings. *Phys. Rev. E* **62**, 993 (2000).

44. V. Ramasubramani, B. D. Dice, E. S. Harper, M. P. Spellings, J. A. Anderson, S. C. Glotzer, freud: A software suite for high throughput analysis of particle simulation data. *Comput. Phys. Commun* **254**, 107275 (2020).

45. A. R. Kansal, T. M. Truskett, S. Torquato, Nonequilibrium hard-disk packings with controlled orientational order. *J. Chem. Phys.* **113**, 4844–4851 (2000).

46. A. Van Blaaderen, J. P. Hoogenboom, D. L. Vossen, A. Yethiraj, A. van der Horst, K. Visscher, M. Dogterom, Colloidal epitaxy: Playing with the boundary conditions of colloidal crystallization. *Faraday Discuss.* **123**, 107–119 (2003).

47. A. Egel, K. M. Czajkowski, D. Theobald, K. Ladutenko, A. S. Kuznetsov, L. Pattelli, SMUTHI: A python package for the simulation of light scattering by multiple particles near or between planar interfaces. *J. Quant. Spectrosc. Radiat. Transf.* **273**, 107846 (2021).

48. D. Theobald, D. Beutel, L. Borgmann, H. Mescher, G. Gomard, C. Rockstuhl, U. Lemmer, Simulation of light scattering in large, disordered nanostructures using a periodic T-matrix method. *J. Quant. Spectrosc. Radiat. Transf.* **272**, 107802 (2021).

49. S. L. Gibbs, C. M. Staller, A. Agrawal, R. W. Johns, C. A. Saez Cabezas, D. J. Milliron, Intrinsic optical and electronic properties from quantitative analysis of plasmonic semiconductor nanocrystal ensemble optical extinction. *J. Phys. Chem. C* **124** (44), 24351–24360 (2020).

50. F. Schulz, O. Pavelka, F. Lehmkühler, F. Westermeier, Y. Okamura, N. S. Mueller, S. Reich, H. Lange, Structural order in plasmonic superlattices. *Nat. Commun.* **11**, 3821 (2020).

51. B. Johs, J. S. Hale, Dielectric function representation by B-splines. *Phys. Status Solidi A* **205**, 715–719 (2008).

52. A. B. Kuzmenko, Kramers–Kronig constrained variational analysis of optical spectra. *Rev. Sci. Instrum.* **76**, 083108 (2005).

53. C. F. Bohren, D. R. Huffman, *Absorption and Scattering of Light by Small Particles* (John Wiley & Sons, Ltd) (1998).

54. J. Xin, J. Zong, J. Gao, Y. Wang, Y. Song, X. Zhang, Extraction and control of permittivity of hyperbolic metamaterials with optical nonlocality. *Opt. Express* **29**, 18572–18586 (2021).

55. P. B. Johnson, R. W. Christy, Optical Constants of the Noble Metals. *Phys. Rev. B* **6**, 4370–4379 (1972).

56. D. M. Pozar, *Microwave Engineering* (John Wiley & Sons) (2011).

57. B. Simpkins, K. P. Fears, W. J. Dressick, B. T. Spann, A. D. Dunkelberger, J. C. Owrutsky, Spanning strong to weak normal mode coupling between vibrational and Fabry–Pérot cavity modes through tuning of vibrational absorption strength. *ACS Photonics* **2**, 1460–1467 (2015).

58. Y. Ying, J. Yu, B. Qin, M. Zhao, T. Zhou, W. Shen, M. Qiu, Q. Li, Directional Thermal Emission Covering Two Atmospheric Windows. *Laser Photonics Rev.* **17**, 2300407 (2023).

59. J. Xu, J. Mandal, A. P. Raman, Broadband directional control of thermal emission. *Science* **372**, 393–397 (2021).

60. C. Lin, Y. Li, C. Chi, Y. S. Kwon, J. Huang, Z. Wu, J. Zheng, G. Liu, C. Y. Tso, C. Y. Chao, B. Huang, A solution-processed inorganic emitter with high spectral selectivity for efficient subambient radiative cooling in hot humid climates. *Adv. Mater.* **34**, 2109350 (2022).

61. D. W. Davies, B. J. Roman, D. J. Milliron, Tuning emittance in films of plasmonic metal oxide nanocrystals for daytime radiative cooling. *Sol. Energy Mater.* **277**, 113094 (2024).

62. G. Li, S. Zhang, T. Zentgraf, Nonlinear photonic metasurfaces. *Nat. Rev. Mater.* **2**, 1–14 (2017).

63. Z. Cai, L. A. Luck, D. Punihaole, J. D. Madura, S. A. Asher, Photonic crystal protein hydrogel sensor materials enabled by conformationally induced volume phase transition. *Chem. Sci.* **7**, 4557–4562 (2016).

64. Z. Sakotic, A. Ware, M. Povinelli, D. Wasserman, Perfect Absorption at the Ultimate Thickness Limit in Planar Films. *ACS Photonics* **10**, 4244–4251 (2023).

65. Z. Wu, B. Liu, S. Liao, Z. Xu, Vibrational strong coupling between graphene plasmons and organic molecules facilitated by perfect absorbers. *Opt. Laser Technol.* **179**, 111370 (2024).

66. Z. T. Brawley, S. D. Storm, D. A. Contreras Mora, M. Pelton, M. Sheldon, Angle-independent plasmonic substrates for multi-mode vibrational strong coupling with molecular thin films. *J. Chem. Phys.* **154** (2021).

67. L. Zhang, H.-J. Xie, Electric field effect on the second-order nonlinear optical properties of parabolic and semiparabolic quantum wells. *Phys. Rev. B* **68**, 235315 (2003).

68. F. Liu, B. Song, G. Su, O. Liang, P. Zhan, H. Wang, W. Wu, Y. Xie, Z. Wang, Sculpting extreme electromagnetic field enhancement in free space for molecule sensing. *Small* **14**, 1801146 (2018).

69. C. Yeh, C. W. Chow, Y. Wu, Y. Lin, B. Cheng, J. Chen, Using optimal cavity loss and saturable-absorber passive filter for stable and tunable dual-wavelength erbium fiber laser in single-longitudinal-mode operation. *Laser Phys. Lett.* **8**, 672 (2011).

70. D. Cricchio, E. Fiordilino, Wavelet analysis and HHG in nanorings: their applications in logic gates and memory mass devices. *Nanoscale* **8**, 1968–1974 (2016).

71. G. Marino, D. Rocco, C. Gigli, G. Beaudoin, K. Pantzas, S. Suffit, P. Filloux, I. Sagnes, G. Leo, C. De Angelis, Harmonic generation with multi-layer dielectric metasurfaces. *Nanophotonics* **10**, 1837–1843 (2021).

72. T. Stolt, J. Kim, S. Héron, A. Vesala, Y. Yang, J. Mun, M. Kim, M. J. Huttunen, R. Czaplicki, M. Kauranen, J. Rho, P. Genevet, Backward phase-matched second-harmonic generation from stacked metasurfaces. *Phs. Rev. Lett.* **126**, 033901 (2021).

73. X. Wen, G. Li, C. Gu, J. Zhao, S. Wang, C. Jiang, S. Palomba, C. Martijn de Sterke, Q. Xiong, Doubly enhanced second harmonic generation through structural and epsilon-near-zero resonances in TiN nanostructures. *Acs Photonics* **5**, 2087–2093 (2018).

74. M. Hensen, T. Heilpern, S. K. Gray, W. Pfeiffer, Strong coupling and entanglement of quantum emitters embedded in a nanoantenna-enhanced plasmonic cavity. *ACS Photonics* **5**, 240–248 (2018).

75. O. S. Ojambati, R. Chikkaraddy, W. D. Deacon, M. Horton, D. Kos, V. A. Turek, U. F. Keyser, J. J. Baumberg, Quantum electrodynamics at room temperature coupling a single vibrating molecule with a plasmonic nanocavity. *Nat. Commun.* **10**, 1049 (2019).

76. A. Faraon, I. Fushman, D. Englund, N. Stoltz, P. Petroff, J. Vučković, Coherent generation of non-classical light on a chip via photon-induced tunnelling and blockade. *Nat. Phys.* **4**, 859–863 (2008).

77. C. Ye, S. Chen, J. Liao, Y. S. Zhang, X. Wang, Y. Song, Efficiently Enhanced Triplet–Triplet Annihilation Upconversion Boosted by Multibandgaps Photonic Crystals. *J. Phys. Chem. C* **124**, 18482–18489 (2020).

78. B. Gu, S. Mukamel, Optical-cavity manipulation of conical intersections and singlet fission in pentacene dimers. *J. Phys. Chem. Lett.* **12**, 2052–2056 (2021).

79. A. Thomas, L. Lethuillier-Karl, K. Nagarajan, R. M. Vergauwe, J. George, T. Chervy, A. Shalabney, E. Devaux, C. Genet, J. Moran, T. W. Ebbesen, Tilting a ground-state reactivity landscape by vibrational strong coupling. *Science* **363**, 615–619 (2019).

80. G. Garcia, R. Buonsanti, E. L. Runnerstrom, R. J. Mendelsberg, A. Llordes, A. Anders, T. J. Richardson, D. J. Milliron, Dynamically modulating the surface plasmon resonance of doped semiconductor nanocrystals. *Nano Lett.* **11**, 4415–4420 (2011).

81. Y. Yao, R. Shankar, M. A. Kats, Y. Song, J. Kong, M. Loncar, F. Capasso, Electrically tunable metasurface perfect absorbers for ultrathin mid-infrared optical modulators. *Nano Lett.* **14** (11), 6526–6532 (2014).

82. S. Doshi, A. Ji, A. I. Mahdi, S. T. Keene, S. P. Selvin, P. Lalanne, E. A. Appel, N. A. Melosh, M. L. Brongersma, Electrochemically mutable soft metasurfaces. *Nat. Mater.* (2024), doi:10.1038/s41563-024-02042-4.

Acknowledgments

Supplementary Materials

1 Colloidal ITO NC Properties

2 Permittivity Functions Related to NC Stacking and Simulated Permittivity

3 Brownian Dynamics Simulation and SMUTHI Calculation Methods

4 Transfer Matrix Model

5 Low Doped ITO NCs and Their Optical Responses

6 Permittivity Function of NC Layers with Molecular Vibrations

7 Finite Element Method Simulation

8 NC Spectra with Different Doping Concentration

Figs. S1 to S17

Tables S1 to S2

References *1-16*